

Behavior of Linear Reconstruction Techniques on Unstructured Meshes

Michael Aftosmis,* Datta Gaitonde,[†] and T. Sean Tavares[‡]

U.S. Air Force Wright Aeronautical Laboratories, Wright-Patterson Air Force Base, Ohio 45433-7913

This paper presents an assessment of a variety of reconstruction schemes on meshes with both quadrilateral and triangular tessellations. The investigations measure the order of accuracy, absolute error, and convergence properties associated with each method. Linear reconstruction approaches using both Green-Gauss and least-squares gradient estimation are evaluated against a structured MUSCL scheme wherever possible. In addition to examining the influence of polygon degree and reconstruction strategy, results with three limiters are examined and compared against unlimited results when feasible. The methods are applied on quadrilateral, right triangular, and equilateral triangular elements to facilitate an examination of the scheme's behavior on a variety of element shapes. The numerical test cases include well-known internal and external inviscid examples and also a supersonic vortex problem for which there exists a closed-form solution to the two-dimensional compressible Euler equations. Such investigations indicate that the least-squares gradient estimation provides significantly more reliable results on poor quality meshes. Furthermore, limiting only the face normal component of the gradient can significantly increase both accuracy and convergence while still preserving the integral cell average and maintaining monotonicity. The first-order method performs poorly on stretched triangular meshes, and analysis shows that such meshes result in poorly aligned left and right states for the Riemann problem. The higher average valence of a vertex in the triangular tessellations does not appear to enhance the wave propagation, accuracy, or convergence properties of the method. Typically, quadrilateral elements provide superior or equivalent discrete solutions with approximately 50% fewer edges in the domain two-dimensional. However, on very poor quality meshes, the triangular elements routinely yield superior accuracy as a result of the trapezoidal quadrature of the Galerkin portion of the numerical flux function.

I. Introduction

THE recent success of characteristic-based upwind differencing on structured meshes has spawned significant research into adopting such methods for use in unstructured adaptive mesh flow solvers.¹⁻⁴ Several basic approaches for the construction of characteristic-based unstructured flow solvers have evolved in recent years. To first order, the support stencils employed in most of these methods are similar in that they rely only on next-neighbor information in a manner that mimics first-order structured schemes. The essential difference in the design of these methods lies in their extension to higher order spatial accuracy.

One approach towards obtaining higher order begins with constructing what is essentially the structured difference stencil on the unstructured mesh. References 2 and 4, for example, use either Harten's modified flux approach⁵ or van Leer's MUSCL⁶ reconstruction to obtain higher order accuracy. Such schemes typically make use of one additional point beyond the nearest neighbor in their difference stencils. Passing this information through the unstructured mesh is the essential challenge faced in their design and implementation. This noncompactness introduces additional complexity into the methods and usually requires additional storage to overcome. A main benefit of this approach is that the resulting schemes generally retain the favorable convergence, robustness, and accuracy properties associated with upwind schemes on structured meshes.²

A second technique was introduced by Ref. 1 using a centered approximation for estimation of the slope within each control volume,

and thus obtains higher order accuracy without informational inquiries beyond the nearest neighbor. Green's theorem approach adopted by Barth's linear reconstruction¹ essentially degenerates to the Fromm scheme in one dimension.⁷ Variations on this theme have been proposed by Ref. 3 and others. Additionally, the concept of using a nearest-neighbor-based slope estimation was immediately generalized to use least squares, constrained least squares, and higher order procedures.⁸⁻¹⁰

Relying only upon next-neighbor information maintains a compactness comparable to central difference based schemes and permits the use of edge-based—and other compact—data structures. A main strength of this class of methods is that they avoid the ambiguities associated with the mapping of structured mesh based difference stencils onto an unstructured mesh and data structure.¹¹

A second important strength stems from the divestment of the gradient calculation from the stencil associated with the Riemann solver. The method requires only a best estimate of the solution gradient within each control volume, and while the surface integral used in linear reconstruction still suffers on poor quality meshes, more elaborate gradient estimations may not. Such procedures may provide dramatically more reliable gradient estimates and suggests the possibility of constructing schemes with much greater tolerance for poor quality meshes. This point becomes increasingly important when considering viscous simulations.¹² In such cases, accurate evaluations of the second derivatives often place severe restriction on the quality of acceptable meshes, and the high aspect ratio cells necessary to resolve the stiff physics of high-Reynolds-number viscous flow may actually hinder accurate gradient estimates. One goal of the present work is to examine the scheme's behavior in detail on the right triangular meshes often employed to resolve viscous layers.

An abundance of research in the recent literature has attempted to capitalize on the promises of various reconstruction techniques. Nevertheless, outstanding questions concerning convergence, accuracy, robustness, and monotonicity remain. The present effort focuses on the simulation of inviscid flow with Roe's approximate Riemann solver. Time integration is achieved via a three-stage modified Runge-Kutta method. The investigations are specifically

Received Sept. 6, 1994; revision received April 20, 1995; accepted for publication May 4, 1995. This paper is declared a work of the U.S. Government and is not subject to copyright protection in the United States.

*Research Scientist; currently NASA Ames Research Center, Mail Stop T27B-2, Moffett Field, CA 94035. Member AIAA.

[†]Visiting Scientist, UES, Inc., WL/FIMC, Bldg. 450, 2645 Fifth Street, Suite 7. Senior Member AIAA.

[‡]NRC Fellow; currently Senior Engineer, Fluid Dynamic Systems Group, Northern Research and Engineering Corporation, 39 Olympia Avenue, Woburn, MA 01801-2073. Senior Member AIAA.

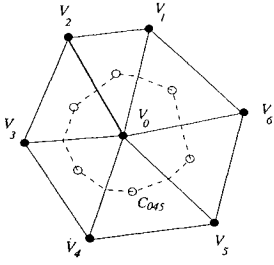


Fig. 1 Unstructured triangular mesh surrounding vertex V_0 .

designed to examine the accuracy, stability, and expense of the various reconstruction algorithms, and comparisons with structured MUSCL schemes are provided wherever possible. The methods are examined on meshes consisting of quadrilateral, right triangular, and equilateral triangular elements to examine the effects of polygon shape on convergence and accuracy. Both Green–Gauss and least-squares reconstructions are considered using Barth’s original limiter,¹ Venkatakrishnan’s limiter,⁷ and a new directional limiter that is presented in Sec. II of this paper.

The investigations are designed to independently examine the methods in a controlled setting. In addition to several well-known numerical test cases, these examples also include problems for which there exist closed-form solutions to the two-dimensional compressible Euler equations. Such cases facilitate quantitative statements about scheme performance and order of accuracy.

II. Theoretical Model

The governing equations are written in flux-integral form:

$$\iint_A \frac{\partial}{\partial t} U \, dA = - \oint_S \bar{\bar{F}} \cdot \mathbf{n} \, dS \quad (1)$$

where U is the state vector of conserved variables and $\bar{\bar{F}}$ is the tensor of flux density containing the inviscid components of the Navier–Stokes equations. This equation may be discretized on an unstructured mesh containing polygons of arbitrary degree. Figure 1 shows a small region of a typical mesh with triangular elements. The present work adopts a node-based approach and thus the flow variables reside at the mesh vertices. The solution procedure for Eq. (1) consists of reconstruction, flux quadrature, and updating of the state variables. The flux quadrature requires evaluation of a divergence operator, whereas the reconstruction step necessitates estimation of a gradient.

A. Formulation

We begin by deriving the edge formulas for the reconstruction as in Ref. 13. This is useful since the analysis contained in subsequent sections will examine many of these expressions and assumptions in significant detail. In Fig. 1, the perimeter of the polygon formed by the set of triangles containing V_0 as a common vertex forms the closed path of integration S . The polygon enclosed by this boundary has an area A equal to the sum of the areas of the figures that share the common vertex V_0 . Thus, the integral path for any given point is chosen to be that described by joining all adjacent points as defined by the edge-to-edge connections. Applying Green’s theorem in the plane then provides an evaluation of the gradient of a passive scalar ϕ at the vertex V_0 ,

$$\iint_A \nabla \phi \, dA = \oint_S \phi \hat{\mathbf{n}} \, dS \quad (2)$$

where $\hat{\mathbf{n}}$ denotes the outward facing local unit normal to S . On the multifaceted control volume shown in Fig. 1, the trapezoidal rule provides a discrete analog to Eq. (2) and is exact if ϕ is linear. The contribution of each edge $V_i V_j$ to the gradient of ϕ at V_0 is then

$$\frac{1}{2} (\phi_{V_i} + \phi_{V_j}) \mathbf{n}_{V_i V_j} \quad (3)$$

where i and j vary cyclically, $i, j \in \{1, 2, \dots, 6\}$, and $\mathbf{n}_{V_i V_j}$ denotes the surface normal vector to edge $V_i V_j$. Following Ref. 13, separation of the cell-based formula in Eq. (3) into contributions from

each of the edges incident upon V_0 permits re-expressing the integration on an edge basis, and so the trapezoidal evaluation of the path integral in Eq. (2) may be equivalently expressed in terms of contributions associated with each node. For a vertex V_j on the perimeter of the cell surrounding vertex V_0 , this term is, where i , and k are vertices adjacent to j ,

$$\frac{1}{2} \phi_{V_j} (\mathbf{n}_{V_i V_j} + \mathbf{n}_{V_j V_k}) \quad (4)$$

To further facilitate application in an edge-based setting, the vectors in Eq. (4) may be written in terms of edges of the centroid dual without changing the actual path of integration S in Eq. (2). Reference 8 points out that

$$\mathbf{n}_{V_i V_j} + \mathbf{n}_{V_j V_k} = 3 \mathbf{n}_{C_{0ij} C_{0jk}} \quad (5)$$

where C_{ijk} denotes the centroid of the triangle formed by vertices V_i , V_j , and V_k . The quadrature of Eq. (2) is evaluated with Eqs. (3–5) to obtain

$$\int_A \nabla \phi \, dA = \oint_S \phi \mathbf{n} \, dS = \sum_{j \in \{V_1, \dots, V_6\}} \phi_{V_j} \frac{3}{2} \mathbf{n}_{C_{0ij} C_{0jk}} \quad (6)$$

with i and k once again denoting the vertices adjacent to j . Hence, the gradient at V_0 may be written as

$$(\nabla \phi)_{V_0} = \frac{3}{A} \sum_{j \in \{V_1, \dots, V_6\}} \frac{1}{2} \phi_{V_j} \mathbf{n}_{C_{0ij} C_{0jk}} \quad (7)$$

To further simplify the operations, Eq. (7) can be made symmetric with respect to the contribution of the vertices associated with each edge. This is achieved by noting that if the surface vectors of the control volume sum to zero, the addition of a constant ($\frac{1}{2} \phi_{V_0}$) to the preceding formula does not affect the gradient or divergence. Thus, Eq. (7) may be recast as

$$(\nabla \phi)_{V_0} = \frac{3}{A} \sum_{j \in \{V_1, \dots, V_6\}} \frac{1}{2} (\phi_{V_i} + \phi_{V_0}) \mathbf{n}_{C_{0ij} C_{0jk}} \quad (8)$$

Finally, since the area A_m of the median dual is exactly one third that of S , Eq. (8) becomes

$$(\nabla \phi)_{V_0} = \frac{1}{A_m} \sum_{j \in \{V_1, \dots, V_6\}} \frac{1}{2} (\phi_{V_i} + \phi_{V_0}) \mathbf{n}_{C_{0ij} C_{0jk}} \quad (9)$$

which is the final formula used in the reconstruction.

Minimum-energy or least-squares reconstruction provides an alternative method for estimating the solution gradient within each cell. This reconstruction process seeks to find the gradient vector that minimizes the least-squares error with respect to the integral cell averages of the distance one neighbors. The procedure involves solution of a (usually) overconstrained system of linear equations. The algorithm can be implemented on an edge-by-edge basis at a cost comparable to that of the Green–Gauss formulation. Details of the least-squares procedure may be found in Refs. 9 and 14–16. As with the Green–Gauss gradient estimation, the set of support vertices for any node includes all distance one neighbors of that node. However, the least-squares process generally de-emphasizes more distant data as compared with the Green–Gauss method.

Figure 2 contains a quadrilateral, right triangular, and a (nearly) equilateral triangular mesh. This figure displays not only the physical mesh but also the median duals of each tessellation. These three meshes will be a basis for many of the investigations that follow. In considering the application of Eq. (9) to unstructured meshes containing polygons other than triangles, consider, for example, its evaluation on quadrilateral cells depicted at the top of Fig. 2,

$$(\nabla \phi)_{V_0} = \frac{1}{A_m} \frac{1}{2} \left\{ \phi_{V_1} \mathbf{n}_{C_{0187} C_{0123}} + \phi_{V_3} \mathbf{n}_{C_{0123} C_{0345}} + \phi_{V_5} \mathbf{n}_{C_{0345} C_{0567}} + \phi_{V_7} \mathbf{n}_{C_{0567} C_{0187}} \right\} \quad (10)$$

where the contribution of ϕ_{V_0} has been explicitly canceled. Since the relationship in Eq. (5) is unique to triangles, this formula corresponds only to a midpoint evaluation of the line integral on the

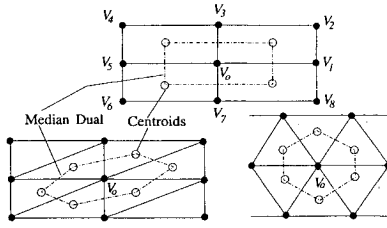


Fig. 2 Physical mesh and median dual for quadrilateral, right triangular, and equilateral triangular tessellations showing support for gradient calculation at control volume surrounding node V_0 .

dotted path shown in Fig. 2. As a result, some of the favorable properties associated with the trapezoidal integration formula have been sacrificed and slightly less tolerance to mesh irregularities may be expected when using the midpoint formula on quadrilateral control volumes.

Once the gradients of the conserved quantities are known, the scalars may be reconstructed throughout the cell:

$$\phi(x, y) = \phi_{V_0} + \nabla \phi \cdot \mathbf{r} \quad (11)$$

where \mathbf{r} is a general vector pointing from V_0 to a point (x, y) . However, such a procedure will not always yield monotonic behavior. Consequently, a limiter Ψ is employed to reduce the slope where necessary:

$$\phi(x, y) = \phi_{V_0} + \Psi \nabla \phi|_{V_0} \cdot \mathbf{r} \quad 0 \leq \Psi \leq 1 \quad (12)$$

Taking Ψ identically equal to zero degenerates the algorithm to first order.

B. Limiters

Barth's¹ original slope limiter is a scalar computed by considering all edges incident upon V_0 and applied directly to $\nabla \phi$. Let $\phi_{r,m}$ be the reconstructed value without limiting at the median point V_m of edge $V_0 V_j$ using the gradient at V_0 :

$$\phi_{r,m} = \phi_{V_0} + \nabla \phi|_{V_0} \cdot \mathbf{r}_{V_0 V_m} \quad (13)$$

Defining $\phi_{\max} = \max(\phi_{V_0}, \phi_{V_j})$, $\phi_{\min} = \min(\phi_{V_0}, \phi_{V_j})$, $\Delta_{1,\max} = \phi_{\max} - \phi_{V_0}$, $\Delta_{1,\min} = \phi_{\min} - \phi_{V_0}$, $\Delta_2 = \phi_{r,m} - \phi_{V_0}$, the scalar Ψ_{0j} associated with the gradient at V_0 due to edge $V_0 V_j$ is

$$\Psi_{0j} = \begin{cases} \min\left(1, \frac{\Delta_{1,\max}}{\Delta_2}\right) & \text{if } \Delta_2 > 0 \\ \min\left(1, \frac{\Delta_{1,\min}}{\Delta_2}\right) & \text{if } \Delta_2 < 0 \\ 1 & \text{if } \Delta_2 = 0 \end{cases} \quad (14)$$

where Ψ is constructed from the various Ψ_{0j} values: $\Psi = \min(\Psi_{0j})$ where j scans all vertices joined to V_0 . This method thus reduces the gradient in all directions equally and pushes Eq. (12) toward first order in all spatial directions. Such scalar limiting reduces both the normal and tangential components of the gradient and results in a relatively dissipative process.

This observation suggests that a less dissipative limiter may be constructed by limiting only the component of $\nabla \phi$ along the surface vector associated with each edge. A directional limiter may be defined in which Ψ does not act isotropically. We begin by resolving the gradient into components normal (\hat{n}) and tangential ($\hat{\tau}$) to an edge of the centroid dual:

$$\nabla \phi = (\nabla \phi \cdot \hat{n})\hat{n} + (\nabla \phi \cdot \hat{\tau})\hat{\tau} \quad (15)$$

The term Ψ is computed in a manner similar to that described earlier but is now applied only to the component of the gradient normal to the edge of the dual:

$$\nabla \phi = \Psi[(\nabla \phi \cdot \hat{n})\hat{n}] + (\nabla \phi \cdot \hat{\tau})\hat{\tau} \quad (16)$$

The limited gradient still ensures a new maximum is not created along the edge and yet it now avoids unnecessarily degrading the tangential component of the slope.

In an attempt to further reduce the severity of limiting, a face-based implementation of this directional limiting was examined. With this approach, the limiting is performed locally for each face separately without influencing the gradient stored at the nodes. Thus, the limiting at any one face of a control volume on the dual mesh occurs independently of any limiting that may be necessary on the other faces. This procedure is analogous to that on a structured mesh where the limiter is applied sequentially in the mesh directions. The process does not preserve the mean of the function value within each cell but can dramatically diminish the number of flux calculations that invoke the limiter. This face-based approach may increase storage requirements somewhat since the limiter must be computed on an edge-by-edge basis. Results with this implementation are unsatisfactory when used in conjunction with Barth's original limiting procedure, and although monotone solutions are produced with low absolute error in one dimension, multidimensional results are erratic. Face-based limiting was not investigated in conjunction with other limiting procedures and is not considered further within this work.

Venkatakrishnan⁷ recently proposed a new limiter designed specifically to enhance the convergence properties of the base scheme. This increase in convergence comes at the expense of strict monotone behavior, as the new (smooth) limiter permits small local overshoots or undershoots in the discrete solution. This limiter may be expressed as

$$\Psi_{0j} = \begin{cases} \frac{1}{\Delta_2} \frac{(\Delta_{1,\max}^2 + \tilde{\epsilon}^2)\Delta_2 + 2\Delta_2^2\Delta_{1,\max}}{\Delta_2^2\Delta_{1,\max}^2 + 2\Delta_2^2 + \Delta_{1,\max}\Delta_2 + \epsilon} & \text{if } \Delta_2 > 0 \\ \frac{1}{\Delta_2} \frac{(\Delta_{1,\min}^2 + \tilde{\epsilon}^2)\Delta_2 + 2\Delta_2^2\Delta_{1,\min}}{\Delta_2^2\Delta_{1,\min}^2 + 2\Delta_2^2 + \Delta_{1,\min}\Delta_2 + \epsilon} & \text{if } \Delta_2 < 0 \end{cases} \quad (17)$$

Here, ϵ is a small number to prevent division by zero whereas $\tilde{\epsilon}$ is chosen to be a variable that controls the degree of limiting and depends on some estimate of mesh scale [$\tilde{\epsilon}^2 = (K\Delta x)^3$]. The term Δx in this formula is defined locally as the diameter of the largest circle that may be inscribed into a particular control volume.

C. Flux Quadrature

The divergence operator required for the flux quadrature of Eq. (1) is closely related to the gradient and consequently follows a similar formulation for each component of the equation. The fluxes are computed in the present work with Roe's flux-difference split method at the midpoint of each edge. First, the state of the flow on either side of the midpoint of each edge is constructed from the known values of the state at each node and the limited gradients computed with the preceding procedure. The flux function is then evaluated and appropriately scattered and accumulated to form the solution change at each node.

III. Results and Investigations

The investigations examine issues of accuracy, convergence, and efficiency with respect to variation in the limiter, type of gradient estimation, and the degree and quality of the control volumes in the discretized domain. These studies are conducted against a backdrop of widely computed numerical test cases and closed-form analytic solutions to the governing equations. In an effort to ensure that the conclusions drawn are general in nature, the numerical examples consider a variety of smooth and nonsmooth internal and external flows. Wherever possible, efforts are made to compare the unstructured results with those from a structured Roe/MUSCL solver.

A. Convergence and Efficiency

Supersonic internal flow through a channel with a 4% circular arc bump provides an initial assessment of the convergence properties of the various methods. Convergence behavior shows very little dependence upon the reconstruction procedure and results are only presented using Green-Gauss.

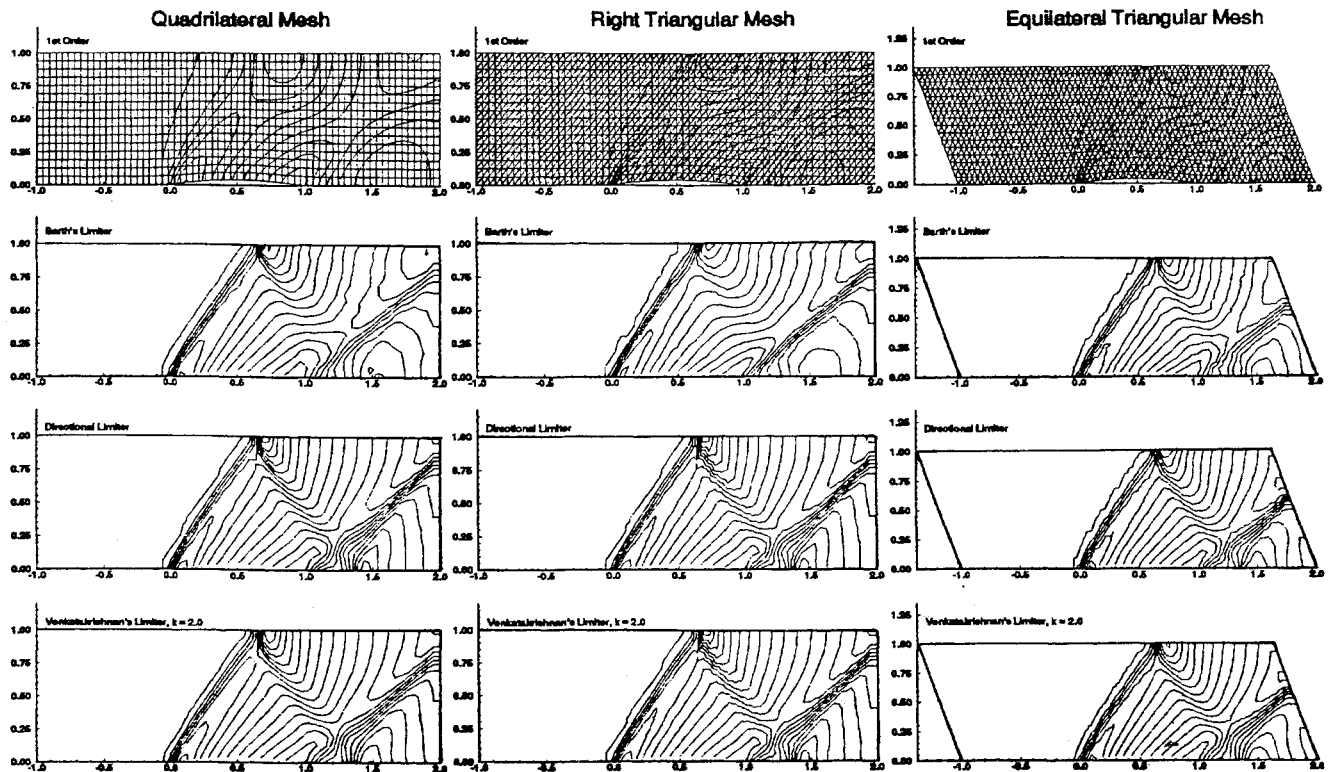


Fig. 3 Density contours for supersonic, inviscid flow through channel with 4% circular arc: $M_\infty = 1.4$ and 65×17 mesh.

Figure 3 introduces this example through density contours showing the three tessellations of a 65×17 mesh. This widely computed test case considers Mach 1.4 freestream flow that enters the duct and sets up an inviscid shock reflection pattern within the domain.¹⁷ The meshes shown in Fig. 3 consist of quadrilateral, right triangular, and equilateral triangular elements, and the cases were computed with both first-order ($\nabla\phi \equiv 0$) upwinding and linear reconstruction with all three of the limiters outlined in Sec. II.B.

All of the cases were run at a Courant–Friedrichs–Lewy number (CFL) of 0.75 with local time stepping, and on all of the meshes, the diffusive character of first-order upwind solutions is apparent. Although all of the methods capture the overall lambda shock structure within the duct, the resolution of the interaction region near the trailing edge permits discrimination among the higher order discrete solutions. On each of the meshes, for example, the directional application of Barth's limiter improves the resolution of this region considerably over the scalar implementation. This is consistent with the observation alluded to in Sec. II.B, where it was suggested that limiting only the component normal to the control volume face would result in a less dissipative operator.

Figure 4 shows convergence histories in the L_1 norm for this case on all three meshes. All of the examples with Venkatakrishnan's limiter used a value of the free parameter K of 2.0. On both triangular meshes, variation of this parameter by more than about ± 0.5 resulted in poor convergence. Convergence behavior on the quadrilateral meshes did not begin to degenerate until this parameter was increased beyond 5.0.

1. Convergence

Looking strictly at the convergence histories it would at first appear that neither Barth's original limiter nor the directional limiter allow the calculations to converge convincingly. However, an examination of the contour plots at several points in the convergence history revealed that these fluctuations manifest themselves only as small amplitude wiggling of the contours about a steady state as has been reported by other investigations.⁷ For the directional limiter, the fluctuations are about an order of magnitude smaller, and perturbations of the contour lines are not immediately evident (although undoubtedly there). This is consistent with the results displayed by the convergence histories. The directional limiter enhanced con-

vergence by roughly an additional order of magnitude, obviously indicating less activity.

One plausible explanation for this behavior views these fluctuations in the convergence histories as the results of sporadic firing of the limiter, thus preventing absolute convergence. This assertion is further supported by the work of Ref. 7, where the free parameter K in Venkatakrishnan's limiter was introduced to prevent the limiter from prematurely reacting to slight oscillations. In the present examples, incorporation of this tolerance facilitates convergence to machine zero on all three meshes (32-bit machine). The directional limiter displays behavior similar to that of Barth. However, in all of the cases, the fact that it only retards one component of the gradient results in somewhat better convergence since the limiting is less severe. This issue will be revisited in the next investigation, where the behavior of each of the limiters is mapped out in detail.

2. Note on Efficiency

As a final note, it is worth mentioning that although all three meshes require roughly the same number of iterations to converge, the calculations on the triangular meshes were 50% more expensive in both memory and time than those on the quadrilateral meshes. This follows since the scheme proceeds on an edge-by-edge basis and six edges (instead of four) are incident upon each vertex in the interior of the mesh. In three dimensions, a typical interior vertex has six incident edges on hexahedral meshes, whereas a corresponding vertex will have approximately 12–14 incident edges on a tetrahedral mesh. Thus, about 2–2.5 times the storage will be needed if a tetrahedral mesh is chosen. The hope is, of course, that the additional edges and flux evaluations in triangular and tetrahedral domains may enhance the wave propagation within the discrete domain and lead to more accurate numerical solutions. Nevertheless, an examination of Fig. 3 does not reveal any obvious benefit stemming from the additional edges present in the tessellation, and it is difficult to justify the additional expense based strictly upon accuracy arguments.

B. Order of Accuracy and Absolute Error

1. Supersonic Vortex

Although the example in the previous section gives some basis for comparing the methods, quantitative measurement of the order

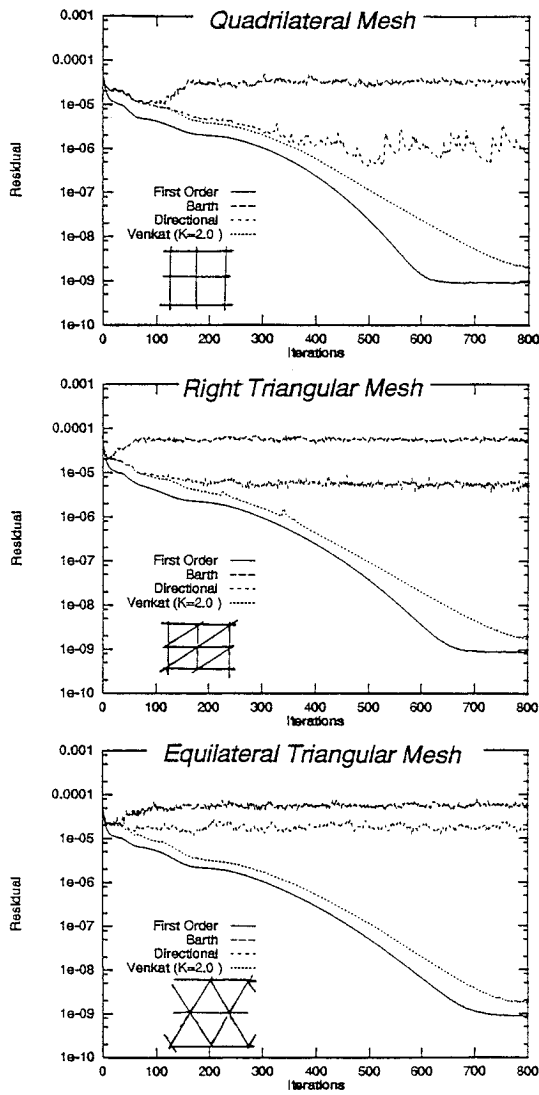


Fig. 4 Convergence histories for various schemes on each mesh for supersonic inviscid flow through channel with 4% circular arc: CFL = 0.75.

of accuracy and discretization error associated with each scheme is best performed on a test case for which an exact, closed-form, analytic solution exists. Examination of a two-dimensional supersonic vortex provides just such an opportunity. Since this is a shock-free compressible flow, the measured order of accuracy is not corrupted by limiter action near shocks and the behavior will correspond to what one may expect of each method in smooth regions of the flow. Using this case as a diagnostic tool permits direct examination of the effects of polygons of various shapes and degrees and also provides an opportunity to study the tolerance of the methods to poor quality meshes.

The inviscid supersonic flow of a compressible fluid between concentric circular arcs presents a flow in which the velocity varies inversely with the radius and the entropy is constant. This flow is a particularly useful test case for upwind methods since the numerical solutions must propagate infinitesimally weak waves accurately to perform the large turning without disrupting the radial flow distribution or introducing shocks. This flow is also of some practical interest as it has been used as a segment of the flow distribution in designing passages for the supersonic blading of compressors and turbines,^{18,19} as well as for a supersonic through-flow fan stage.²⁰

The expression for density ρ as a function of radius r is given by

$$\rho(r) = \rho_i \left[1 + \frac{\gamma - 1}{2} M_i^2 \left\{ 1 - \left(\frac{r_i}{r} \right)^2 \right\} \right]^{\frac{1}{\gamma - 1}} \quad (18)$$

where M_i and r_i are the Mach number and the radius at the inner arc.

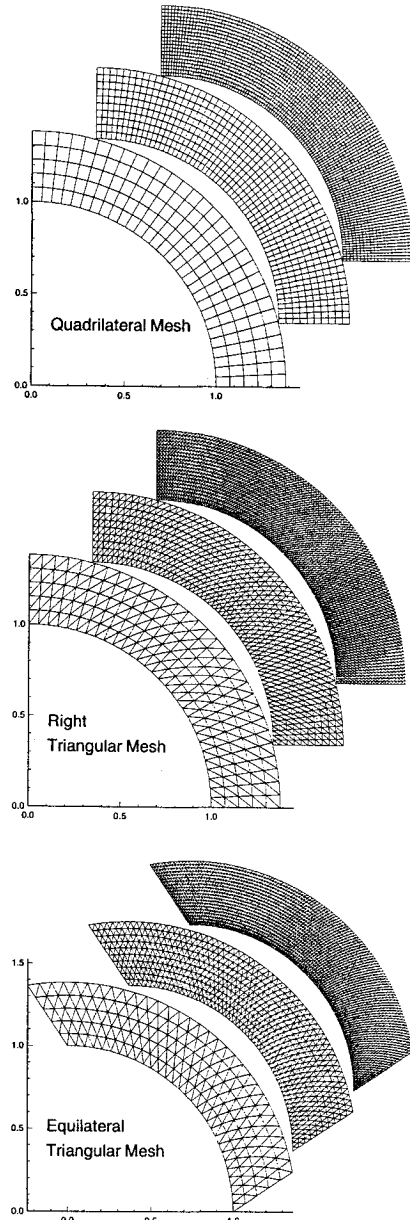


Fig. 5 Sequences of regular meshes used for supersonic vortex.

To evaluate the order of accuracy of each of the methods, a series of discrete solutions to this test case are obtained on the quadrilateral as well as on equilateral and right triangular meshes. For each tessellation, solutions are sought on a set of three telescoping grids with 31×6 , 61×11 , and 121×21 nodes. The Mach number at the inner radius r_i is specified at 2.25 and the outer radius r_o at $1.384 r_i$. Figure 5 shows the three sets of regular meshes used in the simulation. For these regular meshes, the aspect ratio is of order 1.

The simulations are initiated by releasing the inlet profile into a nearly evacuated duct and converged to steady state. Figure 6 displays pressure contours (inc. = 0.25) resulting from the computations on the medium meshes. The extreme diffusivity of the first-order schemes again becomes apparent in these plots, and the pressure in the first-order simulations drops dramatically along streamlines as the flow proceeds around the duct. Some evidence of dissipation is also evident in the higher order discrete solutions, but it is not nearly as pronounced as in the first-order cases. Convergence behavior for all of the schemes mimics that for the duct flow case presented earlier. The noise in the solutions with the first two limiters will be discussed shortly.

The existence of an exact solution to this problem makes it possible to directly compute distributions of error throughout the domain.

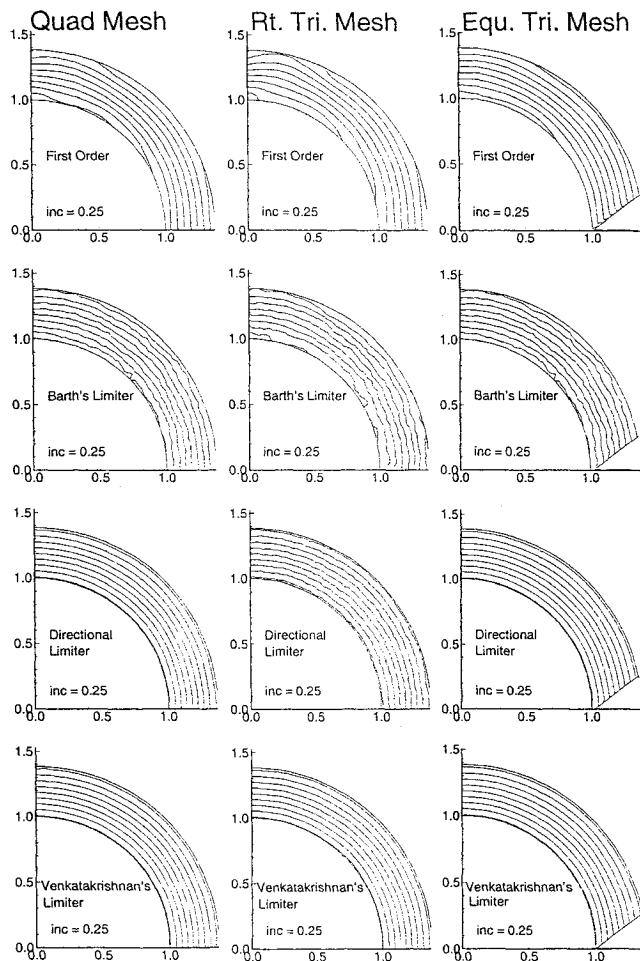


Fig. 6 Pressure contours on medium meshes with various reconstruction methods and limiters: $M_{in} = 2.25$, $\rho_{in} = 1$, $p_{in} = 1/\gamma$, $r_i = 1$, and $r_o = 1.384$.

Figure 7 contains contour plots of density error for the medium triangular and quadrilateral meshes for all of the methods. Each contour level indicates 2% error in the local density distribution. Note that the error contours do not display any anomalies approaching the walls or boundaries, suggesting that the accuracy near the wall is the same as that in the interior of the field.

By comparing the error in the discrete solutions on a successively refined sequence of telescoping meshes, quantitative measurements of both order of accuracy and absolute error are possible. Note that since the simulations were run to convergence, the error measured is not directly truncation error but rather the error in the discrete solutions. The Appendix tabulates the L_1 and L_2 norm of the density error in the discrete solutions on all of the meshes considered in this example. In addition, it offers order of accuracy estimates for the procedures on each type of polygon. In general, the L_1 and L_2 norms behave quite similarly, and the order of accuracy of the discrete solutions is roughly the same in using either measure. Since the L_2 norm is more sensitive to extrema, this fact suggests that discretization error is being driven out of the domain uniformly and supports the contention that the boundaries are free from anomalies. Selected data will be extracted from these tables to aid in the analysis of the following sections.

2. Polygon Degree

The first investigation examines the influence of the shape and degree of the polygons in the domain on the accuracy of the discrete solutions. Since results free from the effects of limiters are sought, the simulations are started from the exact solution, and discrete solutions are obtained without the use of flux limiters. The order of accuracy of the discrete method is assessed by performing a linear regression on log-log plots of absolute density error in both L_1 and

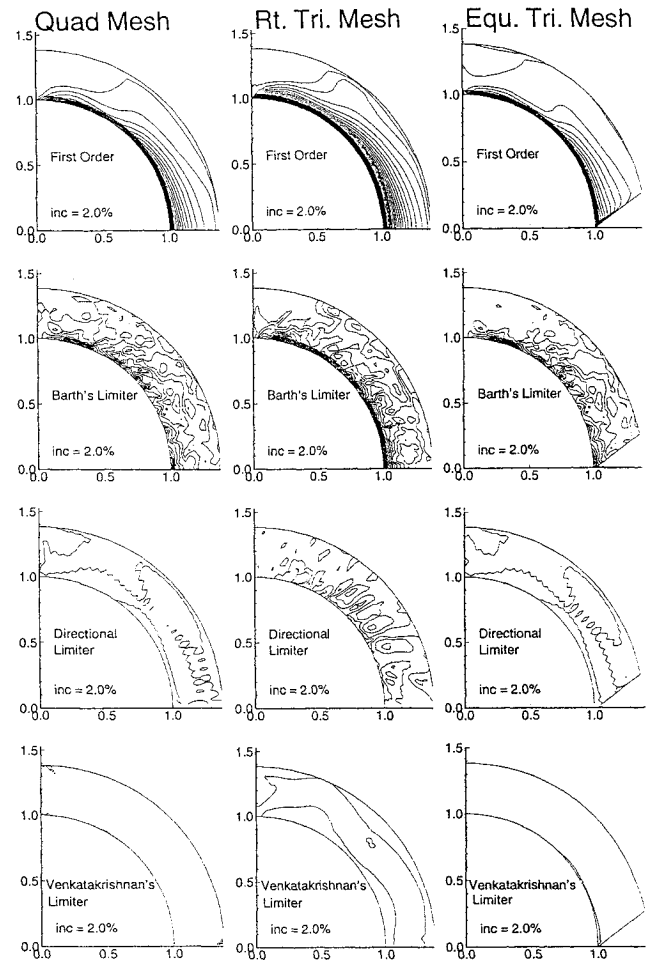


Fig. 7 Contours of density error on medium meshes for supersonic vortex test case, contours drawn every 2%: $M_{in} = 2.25$, $\rho_{in} = 1$, $p_{in} = 1/\gamma$, $r_i = 1$, and $r_o = 1.384$.

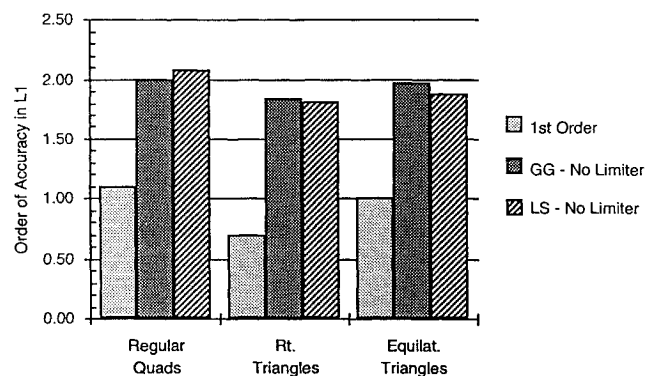


Fig. 8 Order of accuracy of unlimited schemes on regular meshes for the supersonic vortex problem.

L_2 norms vs normalized grid spacing represented by the reciprocal square root of the number of nodes in the domains. Figure 8 presents the order of accuracy of the methods in L_1 , and Table A1 in the Appendix contains the data used to generate this chart.

In this example, both the order of accuracy and absolute error on the quadrilateral and equilateral triangular tessellations are comparable. The order of accuracy on these two meshes is 5–10% better than that on the right triangular mesh with either reconstruction procedure. The first-order results show a more pronounced deficit, placing the order of accuracy of the right triangular mesh at about 0.7 as compared with 1.1 and 1.0 for the quads and equilateral triangles, respectively. This fact suggests that something in the very nature of the right triangles is responsible for the lower order of accuracy on such meshes.

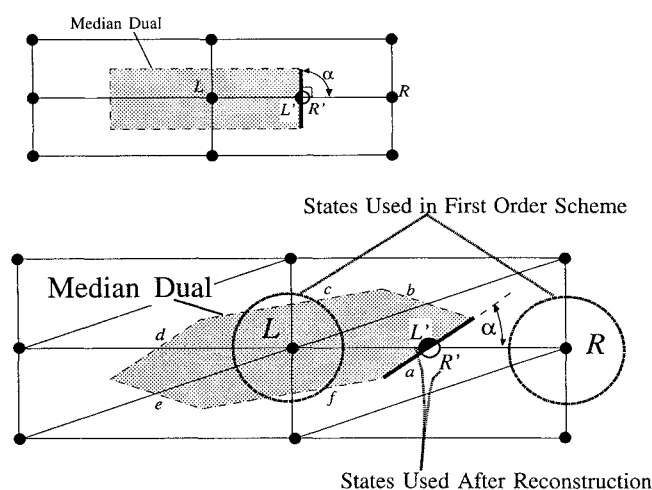


Fig. 9 Setting up of the local Riemann problem on a face of the auxiliary meshes for quadrilateral and right triangular tessellations.

The sketches in Fig. 9 permit a direct comparison of the dual meshes on quadrilateral and right triangular tessellations. In examining this figure it becomes apparent that the face a , which is pierced by the edge LR is at a right angle α on the quadrilateral mesh but not on the stretched triangular mesh. (Note that Fig. 2 shows that α is a right angle on equilateral triangular meshes as well.) In fact, as the mesh stretching increases, the alignment of faces like a , b , d , and e with their respective edges becomes less and less orthogonal.

When the first-order essentially one-dimensional scheme evaluates the flux across a poorly aligned face, like a , the Riemann solver expects data normal to the face, but the data provided by either vertex of edge LR is far removed from the true normal and necessarily introduces an error into the flux evaluation. On unskewed quadrilateral meshes or equilateral triangular meshes, α is very nearly a right angle. As a result, the data introduced into the approximate Riemann solver is well aligned with the normal to the face, and such an error is avoided. Such arguments support the hypothesis that the first-order scheme may degrade rapidly on highly stretched right triangular meshes.

When linear reconstruction is introduced into the formation of the numerical flux, the new left and right states for the Riemann problem are now formed on either side of face a in Fig. 9. These states are labeled L' and R' in the sketch and take into account linear variation within the auxiliary cell. An alternate view of the situation is to realize that the reconstruction step has taken data into account from all of the distance one vertices adjacent to L and R , thus enlarging the stencil to permit information to propagate in the face-normal direction. Since there is no direct edge connection normal to face a , the first-order scheme necessarily makes an error when propagating information against the mesh diagonal. Reconstruction allows the higher order scheme to recover more than the single order of magnitude associated with the slope estimation and very nearly matches the discrete solutions of the quadrilaterals and equilateral triangles. By enlarging the stencil to incorporate data in the face-normal direction, reconstruction reduces the misalignment of the Riemann problem present in the first-order discrete solutions.

Some general comments stem from this investigation with the unlimited schemes on regular meshes. 1) On regular meshes the Green-Gauss and least-squares gradient estimation procedures yield similar results. 2) The regular quadrilateral and equilateral meshes yield very similar discrete solutions, both in order of accuracy and absolute magnitude of the error. Nevertheless, the simulations on quadrilaterals require approximately 50% less storage and CPU simply by virtue of the fact that fewer edges exist in the domain. 3) The scheme seems to treat right triangles as distorted equilateral triangles and increases the reliance on the gradient estimation for the production of accurate discrete solutions.

Table 1 Severity and frequency of limiter firing after practical convergence—average values on medium mesh for supersonic vortex flow

Barth's limiter			
Edges limited, %		Mean Ψ	
GG	LS	GG	LS
18.32677	16.62402	0.2444862	0.2487914
17.01772	15.99409	0.2593847	0.2473031
16.63386	18.34646	0.2549107	0.2249657
19.19291	16.70275	0.2311892	0.2505058
17.70669	15.86614	0.2648712	0.2523419
16.80118	17.42126	0.2390375	0.2494676
18.58268	15.75787	0.2293676	0.2628614
17.14567	15.59055	0.2513207	0.2808488
16.68307	17.02756	0.2457611	0.2357707
18.24803	15.93504	0.2329683	0.2580887

Directional limiter			
Edges limited, %		Mean Ψ	
GG	LS	GG	LS
24.72441	24.58661	0.9240345	0.9457827
24.72441	24.57677	0.9240335	0.9457660
24.72441	24.57677	0.9240359	0.9457663
24.72441	24.57677	0.9240357	0.9457676
24.72441	24.55709	0.9240360	0.9457363
24.72441	24.56693	0.9240357	0.9457521
24.72441	24.56693	0.9240364	0.9457527
24.72441	24.56693	0.9240357	0.9457538
24.72441	24.54725	0.9240348	0.9457356
24.72441	24.56693	0.9240317	0.9457530

Venkatakrishnan limiter, $K = 10$			
Edges limited, %		Mean Ψ	
GG	LS	GG	LS
6.072834	4.970472	0.9779245	0.9867367
6.072834	4.970472	0.9779246	0.9867366
6.072834	4.970472	0.9779246	0.9867365
6.072834	4.970472	0.9779242	0.9867367
6.072834	4.970472	0.9779242	0.9867365
6.072834	4.970472	0.9779242	0.9867368
6.072834	4.970472	0.9779245	0.9867368
6.072834	4.970472	0.9779246	0.9867369
6.072834	4.970472	0.9779245	0.9867367
6.072834	4.970472	0.9779245	0.9867367

3. Limiter Behavior

The next set of numerical examples introduces the slope limiters into the simulations on the three sets of regular meshes previously presented. This investigation is designed to quantitatively compare the effects of limiting on scheme accuracy with each of the three polygons types.

As mentioned earlier, the limiter originally proposed for the scheme¹ is a scalar corresponding to the severest requirement that maintains monotonicity. The directional implementation of this limiter was presented in Sec. II.B and is designed to reduce the severity of the limiting by decreasing only the normal component of the gradient. The third limiter examined was recently proposed by Venkatakrishnan.⁷ This smooth limiter is less severe, and is invoked less frequently than Barth's original limiter.

After converging numerical simulations on the medium quadrilateral mesh for about 10,000 iterations to reach a steady state, the behavior of the limiter with each scheme was monitored for several hundred iterations. Table 1 contains an excerpt from this data and tracks the mean behavior of each limiter for several iterations. The first two columns display the percentage of all edges within the domain on which the limiter was applied for each reconstruction method. The last two columns tabulate the average value of the limiter on only those faces where the limiter was active, thus giving a picture of the severity of the limiting taking place. Of course, since the discrete answers are slightly different, the edges with flux evaluations that invoke the limiter are not always the same from solution

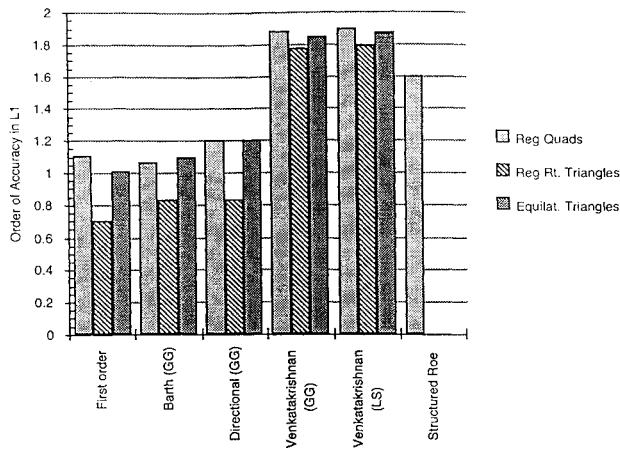


Fig. 10 Order of accuracy of limited schemes on regular polygons for the supersonic vortex problem.

to solution. The lack of absolute convergence with Barth's limiter is immediately apparent in the first two columns as the number of limited edges changes from time step to time step but hovers around 17%. The average value of the limiter on these edges is around 0.25, indicating a very nearly first-order flux evaluation on these edges. Applying this limiter only to the normal component of the gradient substantially reduces the magnitude of the slope degradation as shown by the tabulated results with the directional limiter. With this vector application of Barth's limiter, the limited slopes retain 92–94% of their magnitude and monotonicity is still guaranteed. The fact that the exact number of limited edges is now substantially more stable gives evidence of the deeper convergence afforded by the milder limiting. Venkatakrishnan's limiter is designed to fire less frequently, and this table shows that with $K = 10$ it is triggered on only 5–6% of the edges, depending on the reconstruction, and reduces the slopes by an average of only 2–3%.

Figure 10 summarizes the effects of limiting on the order of accuracy with the regular meshes of each polygon shape. These results summarize the data contained in Table A2 in the Appendix, which presents both error norms and order of accuracy estimates. Figure 10 shows that Venkatakrishnan's limiter nearly reproduces the behavior of the unlimited schemes for this smooth flow. This is consistent with the high values of the limiter observed in Table 1.

In cases with no limiting, or with very little limiting—as with Venkatakrishnan's limiter—the right triangular elements almost match the accuracy of the other two tessellations. However, this has come from an increased reliance on the gradient estimation. The behavior with the directional limiter provides a good demonstration of this. When the gradient at L or R is decreased due to limiting, the stencil will again revert to the poorly aligned first-order Riemann solution and the propagation of information will be restricted. Thus, the reconstructed values at the cell face will degrade rapidly. In Eq. (13), accurate estimations of $\phi_{r,m}$ rely ever more heavily on $\nabla\phi$ since ϕ_{v_0} represents data not normal to the face. Thus, limiting $\nabla\phi$ will degrade the discrete solution more severely than on well-aligned meshes. On the finest right triangular mesh with the directional limiter the error is nearly 10 times that on the equilateral triangles or quadrilaterals with the same limiter (see Table A2 in the Appendix).

4. Polygon Quality

Although it is informative to evaluate the scheme's performance on the meshes in the previous investigation, such smooth, regular, aspect ratio ~ 1 polygons are rarely found in practice. Having established a reference level for scheme accuracy, focus now shifts to discrete solutions on stretched and distorted meshes.

Figure 11 displays two sets of telescoping stretched meshes. The quadrilateral and triangular elements were formed on the same set of vertices and the aspect ratio of the (quadrilateral) elements is about 40. The original scalar limiter and the directional limiter refused to converge on the coarse and medium triangular meshes for this case, and so Table A2 in the Appendix only contains results with the first-order scheme and Venkatakrishnan's limiter.

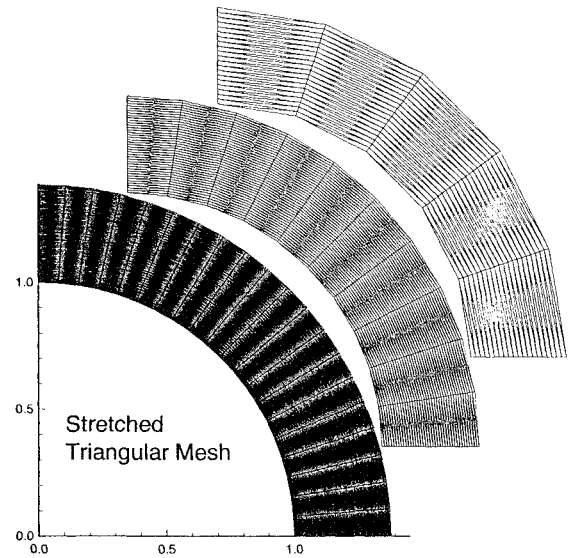
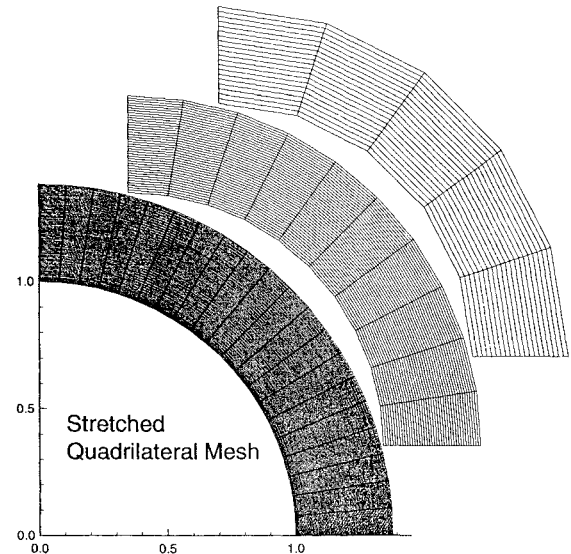


Fig. 11 Sequences of stretched meshes used for supersonic vortex.

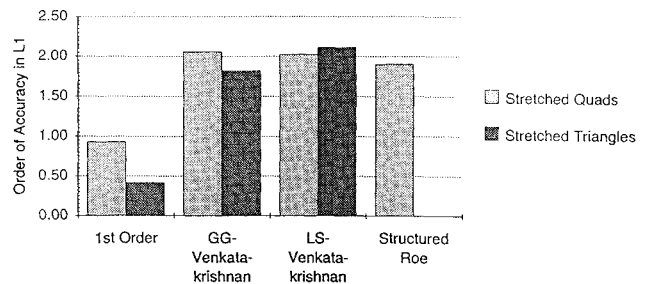


Fig. 12 Order of accuracy of limited schemes on stretched polygons for the supersonic vortex problem.

Figure 12 contains a comparison of the order of accuracy information derived from the tabulated data. The first-order results place the order of accuracy on the quadrilateral cells at 0.93 and the right triangular scheme at only 0.41. Such results are consistent with the argument presented earlier that predicted that the alignment problem becomes worse with increasing cell aspect ratio.

At first glance, the improvement in order of accuracy for the reconstructed solutions on the triangular grid is very impressive. Although the order of accuracy is still 5–10% lower than on the quadrilateral meshes, reconstruction has improved the solution by more than a full order of magnitude. However, after examining the data in Table A3, it is clear that even on the finest mesh the discrete

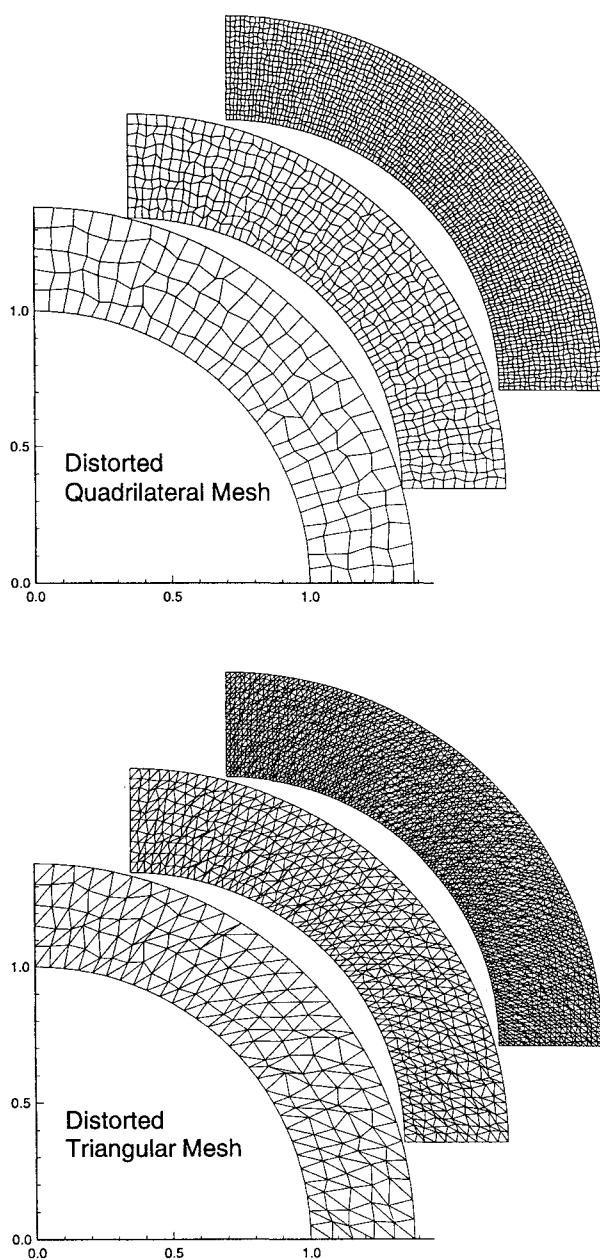


Fig. 13 Sequences of randomly distorted meshes used for supersonic vortex.

solutions on the right triangular mesh exhibit 4–10 times more error than on the quadrilateral tessellation of the same set of nodes. Despite this, the discrete solutions on the fine triangular mesh are quite reasonable, and on a sufficiently fine mesh, the gradient estimation is able to compensate for the error in the first-order scheme.

The right triangle's increased dependency on the accuracy of the gradient estimation becomes apparent when studying the behavior of the discrete solutions on the coarse meshes. On these meshes, only five points spanned the domain in the streamwise direction. The resulting gradient estimates led to discrete solutions that are actually worse than the first-order simulations. On the quadrilateral meshes, similar gradient estimates improved the discrete solutions by a factor of 2–6.

Finally, in regarding Table A3, note that the discrete solution on the right triangular mesh using least-squares reconstruction converged to a result that unstarted the flow. Since it converged to a different physical solution, this point was not considered in the slope estimate provided in the table. The results for this test case appear to substantiate observations made previously. However, the scheme's poor performance on the coarse right triangular mesh suggests that they should be regarded as preliminary until the results can be substantiated by computations on still finer stretched meshes.

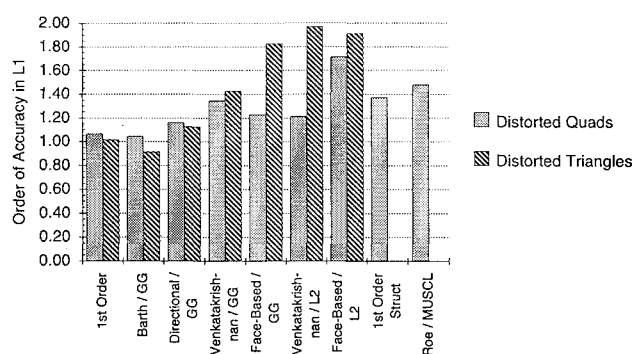


Fig. 14 Order of accuracy of limited schemes on randomly distorted polygons for the supersonic vortex problem.

To examine the scheme's tolerance to distorted elements, the regular meshes shown in Fig. 5 were perturbed to introduce localized skewing. Figure 13 displays the resulting distorted meshes. Each mesh point was randomly displaced within a small region of its local neighborhood. The resultant sets of nodes were then connected to form both quadrilateral and triangular polygons. Notice, that these meshes do not telescope, since the magnitude of the mesh point displacement scales with the normalized mesh spacing.

Figure 14 compares the estimated order of accuracy for each discrete method on the two polygon types. This chart is again drawn from the information provided in the Appendix (Table A4). The chart displays a clear degradation in accuracy on the quadrilateral meshes. The triangular elements, in contrast, produce results that nearly match those on regular equilateral triangles presented earlier. Table A4 shows that, in general, somewhat higher discretization error exists on the distorted triangular meshes. However, this table also shows that the least-squares cases are extremely tolerant to the mesh distortion and the error in these solutions is very nearly as low as that on the regular triangular meshes.

These observations support several general statements about the method's performance on distorted polygons. It appears that on both tessellations, the least-squares gradient estimation is far more capable of producing reliable results on distorted meshes. Moreover, it is also evident that the trapezoidal integration of the Galerkin portion of the numerical flux function on triangles makes these polygons far more tolerant of mesh distortion. The order of accuracy on the distorted quadrilateral meshes degenerates much more quickly, since the edge formulas only result in midpoint quadrature for these polygons. Notice, however, that the absolute magnitude of the error on all of the quad meshes remains very low, which suggests that the coefficient of the discretization error expression remains small.

C. External Inviscid Flow—Transonic NACA 0012 Airfoil

Transonic, inviscid flow past a NACA 0012 airfoil poses a challenging and realistic problem on which to verify the features of the various algorithms discussed in the preceding sections. Mach 0.8 flow at an angle of attack of 1.25 deg results in a steady solution with a slip line at the trailing edge, a strong shock on the suction surface, and a weak shock on the pressure side.

The mesh employed in this example consists of 131×65 vertices, and the circumferential resolution was chosen such that the lower shock just formed when using the Green–Gauss reconstruction in conjunction with Venkatakrishnan's limiter on the quadrilateral mesh. As in the previous examples, the first-order triangular scheme produces a result that is more diffuse than that on the quad mesh. The triangles near the surface are very nearly right triangles with an aspect ratio of roughly 10, and the most likely explanation is again poor alignment of the Riemann solver. Reconstruction dramatically improves the quality of the discrete solutions not only because of the higher order of accuracy of the resulting scheme but also as a result of the extended support stencil used in forming the Riemann problem.

The C_p plots in Fig. 15 provide a more quantitative assessment of the different schemes. This figure contains the results from all tested combinations of limiter and reconstruction method. Also included for reference are results from a cell-centered structured

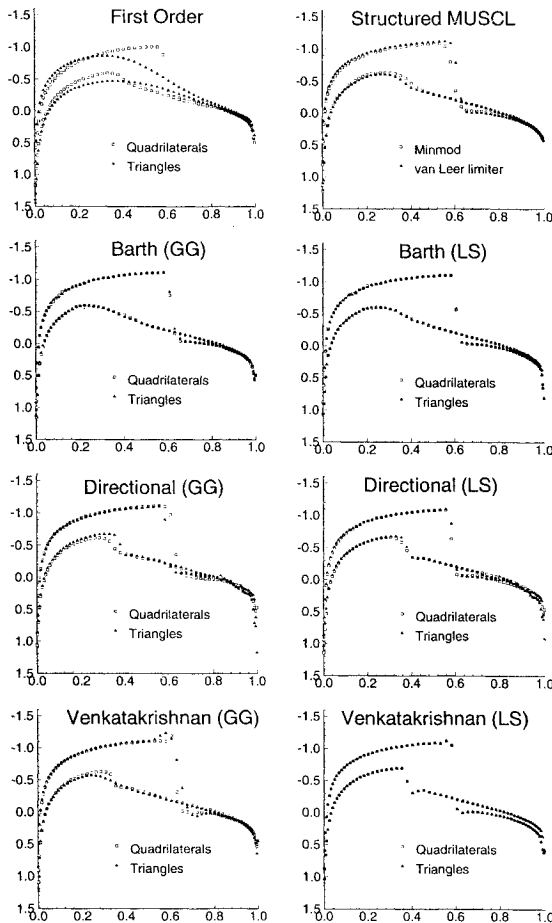


Fig. 15 C_p distributions with various schemes for Mach 0.8 and $\alpha = 1.25$ deg NACA 0012 airfoil.

Roe/MUSCL solver.²¹ The profiles are strongly dependent upon the capturing of the weak lower shock. Less accurate methods fail to predict this shock and represent it as simply a smooth compression. With the exception of the structured mesh results, hollow squares denote data with the quadrilateral meshes, whereas filled triangles represent the triangular elements.

In the first-order solutions, only the quadrilateral mesh gives any indication of the lower shock's existence. On either of these meshes, the original scalar limiter fails to predict the shock as well. Indeed, these results did not converge convincingly, and the residual stalled after dropping approximately three orders of magnitude. The directional implementation of this limiter reduced the residual by an additional two orders, and the lower shock is evident in the discrete solutions on both tessellations. As in the previous examples, Venkatakrishnan's limiter converges to machine zero, but over/undershoots appear in all of the examples.

The behavior of the two reconstruction methods follows the same trends as in the shockless flows considered earlier. The least-squares method appears to produce more accurate gradient estimates, and the advantage is particularly evident on the triangular meshes. This method also shows a reduced sensitivity to polygon shape because it more appropriately weights the data surrounding a vertex. On triangular meshes formed by division of quadrilaterals, the Green-Gauss reconstruction may actually introduce a diagonal bias, whereas the least-squares method reduces the weighting of these points due to their distance from the central vertex. On none of these relatively smooth grids did the additional edge calculations present on the right triangular meshes result in any apparent advantage.

IV. Conclusions

The accuracy and efficiency of a variety of common edge-based reconstruction schemes are examined on unstructured meshes with various limiters and types of polygons. For meshes with cell aspect ratios near one, the accuracy of the discrete solutions on triangles

and quadrilaterals is nearly the same in both order and absolute magnitude. Right triangular elements, however, appear to be viewed as distorted equilateral triangles—with an associated reduction in scheme accuracy that is particularly severe in the piecewise constant, first-order scheme. The situation is exacerbated when the mesh is stretched to produce high aspect ratio elements and the Riemann solver is more poorly aligned with the edge that introduces the first-order data. Higher order calculations on such meshes rely on the reconstruction to extend the support of the first-order stencil. This results in an increased burden on the gradient estimation and makes them easily degraded by limiting. Even when the reconstruction helps recover the loss in order of accuracy, the absolute level of error in the discrete solutions remains a factor of 5–10 higher than on the quadrilateral meshes. The fact that quadrilaterals are not rigid figures makes it possible to stretch these cells without introducing skewing, and elevated cell aspect ratio does not degrade these discrete solutions. Nevertheless, on poor quality meshes, the midpoint integration and smaller support stencil of the quadrilateral meshes combine to make the discrete solutions degenerate more rapidly.

A new directional implementation of Barth's original scalar limiter is introduced that preserves the cell average and retains monotonicity. This approach limits only the component of the gradient normal to the face. Numerical experiments show that this implementation significantly reduces the dissipation introduced by the original scalar procedure. Venkatakrishnan's smooth limiter performs as expected and converges for all test cases while producing small over/undershoots in the discrete solutions. A very promising approach toward further reducing the introduction of excessive dissipation into the solutions may be the directional implementation of Venkatakrishnan's limiter.

On regular and stretched meshes, the additional edges in the triangular meshes do not lead to any apparent accuracy advantage over the quadrilateral scheme. These additional edges, however, do mandate 50% higher (in two-dimensions) storage and CPU requirements (over 200% in three-dimensions) simply by virtue of the tessellation and the fact that the scheme proceeds on an edge basis. These observations support a possible mesh generation strategy that removes unnecessary edges from boundary-layer regions and other regular portions of an unstructured triangular mesh and processes such regions as a collection of mixed quadrilateral and triangular elements.

Appendix: Tabulated Norms of Density Error

Table A1 Error percentages in discrete solutions in L_1 and L_2 norms for supersonic vortex problem on regular meshes without limiting, SS vortex results with limiters turned off

Regular meshes						
Limiter and error norm $1/\sqrt{(\text{No. of nodes})}$	Quad mesh					
	First order		Green-Gauss		Least squares	
	L_1	L_2	L_1	L_2	L_1	L_2
5.42E-02	16.04	24.62	0.87	1.47	0.40	0.47
2.79E-02	7.39	11.04	0.28	0.46	0.10	0.13
1.42E-02	3.65	5.32	0.06	1.10	0.03	0.04
Slope/est. O.A.	1.10	1.14	1.99	2.00	2.08	1.93
Right triangular mesh						
Limiter and error norm $1/\sqrt{(\text{No. of nodes})}$	First order		Green-Gauss		Least squares	
	L_1	L_2	L_1	L_2	L_1	L_2
	L_1	L_2	L_1	L_2	L_1	L_2
5.42E-02	12.41	19.77	0.98	1.66	1.01	1.70
2.79E-02	9.20	14.41	0.26	0.49	0.29	0.51
1.42E-02	4.86	7.51	0.08	1.16	0.09	0.17
Slope/est. O.A.	0.70	0.72	1.83	1.74	1.80	1.71
Equilateral triangular mesh						
Limiter and error norm $1/\sqrt{(\text{No. of nodes})}$	First order		Green-Gauss		Least squares	
	L_1	L_2	L_1	L_2	L_1	L_2
	L_1	L_2	L_1	L_2	L_1	L_2
5.42E-02	7.55	12.95	0.98	1.68	1.09	1.95
2.79E-02	3.84	6.53	0.26	0.46	0.29	0.51
1.42E-02	1.96	3.20	0.07	0.12	0.09	0.17
Slope/est. O.A.	1.01	1.05	1.97	1.95	1.87	1.82

Table A2 Error percentages in discrete solutions to supersonic vortex problem on meshes of regular polygons for schemes with limiting, SS vortex results with flux limiting on

Regular meshes												
Quadrilateral cells												
Limiter and error norm	First order		GG-Barth		GG-directional		GG-Venkatakrisnan		LS-Venkatakrisnan		Structured Roe	
$1/\sqrt{(\text{No. of nodes})}$	L_1	L_2	L_1	L_2	L_1	L_2	L_1	L_2	L_1	L_2	L_1	L_2
5.42E-02	16.04	24.62	6.62	9.80	0.44	0.74	0.93	1.49	0.38	0.63	8.180	9.820
2.79E-02	7.39	11.04	3.40	4.63	0.22	0.52	0.24	0.41	0.09	0.14	2.668	3.233
1.42E-02	3.65	5.32	1.58	2.23	0.09	0.15	0.08	0.13	0.03	0.05	0.964	1.340
Slope/est. O.A.	1.10	1.14	1.07	1.10	1.21	1.19	1.88	1.84	1.89	1.87	1.60	1.49
Right triangular cells												
Limiter and error norm	First order		GG-Barth		GG-directional		GG-Venkatakrisnan		LS-Venkatakrisnan		Structured Roe	
$1/\sqrt{(\text{No. of nodes})}$	L_1	L_2	L_1	L_2	L_1	L_2	L_1	L_2	L_1	L_2	L_1	L_2
5.42E-02	12.41	19.77	9.29	13.97	2.60	3.14	1.00	1.48	0.99	2.05	—	—
2.79E-02	9.20	14.41	5.49	7.28	1.50	1.88	0.31	0.46	0.18	0.30	—	—
1.42E-02	4.86	7.51	3.07	3.84	0.85	1.08	0.09	0.14	0.09	0.17	—	—
Slope/est. O.A.	0.70	0.72	0.83	0.96	0.83	0.80	1.77	1.78	1.79	1.85	—	—
Equilateral triangular cells												
Limiter and error norm	First order		GG-Barth		GG-directional		GG-Venkatakrisnan		LS-Venkatakrisnan		Structured Roe	
$1/\sqrt{(\text{No. of nodes})}$	L_1	L_2	L_1	L_2	L_1	L_2	L_1	L_2	L_1	L_2	L_1	L_2
5.42E-02	15.11	18.22	7.11	11.06	0.44	0.78	1.01	1.47	0.38	0.82	—	—
2.79E-02	7.52	9.02	3.50	5.48	0.23	0.38	0.31	0.46	0.09	0.27	—	—
1.42E-02	3.91	4.45	1.62	2.60	0.09	0.15	0.08	0.13	0.03	0.07	—	—
Slope/est. O.A.	1.01	1.05	1.10	1.08	1.20	1.22	1.85	1.83	1.87	1.82	—	—

Table A3 Error percentages in discrete solutions for supersonic vortex problem on meshes of regular stretched polygons with $AR \approx 40$

Stretched meshes									
Quadrilateral cells									
Limiter and error norm	First order		GG-Venkatakrisnan		LS-Venkatakrisnan		Structured Roe		
$1/\sqrt{(\text{No. of nodes})}$	L_1	L_2	L_1	L_2	L_1	L_2	L_1	L_2	L_2
5.42E-02	19.11	27.43	8.73	12.43	3.69	5.99	13.78	13.02	
2.79E-02	17.64	24.18	2.85	3.60	1.52	1.65	3.64	3.43	
1.42E-02	5.54	8.18	0.56	0.76	0.25	0.38	1.08	1.04	
Slope/est. O.A.	0.93	0.91	2.06	2.08	2.03	2.06	1.90	1.88	
Triangular cells									
Limiter and error norm	First order		GG-Venkatakrisnan		LS-Venkatakrisnan				
$1/\sqrt{(\text{No. of nodes})}$	L_1	L_2	L_1	L_2	L_1	L_2			
5.42E-02	19.56	23.23	28.24	33.66	#40.09#	#48.07#			
2.79E-02	15.52	19.07	13.28	15.61	8.44	9.79			
1.42E-02	11.23	14.57	2.47	2.85	2.36	3.19			
Slope/est. O.A.	0.41	0.35	1.82	1.85	1.88	1.66			

Table A4 Error percentages in discrete solutions to supersonic vortex problem on meshes of randomly distorted polygons as described in text

Regular meshes												
Quadrilateral cells												
Limiter and error norm	First order		GG-Barth		GG-directional		GG-Venkatakrisnan		LS-Venkatakrisnan		Structured Roe	
$1/\sqrt{(\text{No. of nodes})}$	L_1	L_2	L_1	L_2	L_1	L_2	L_1	L_2	L_1	L_2	L_1	L_2
5.42E-02	15.77	23.93	7.05	10.95	1.26	1.79	1.51	2.41	0.97	1.41	8.525	10.38
2.79E-02	7.31	10.79	3.03	4.85	0.57	0.78	0.95	1.54	0.43	0.60	3.077	3.712
1.42E-02	3.79	5.50	1.75	2.59	0.27	0.36	0.25	0.36	0.19	0.26	1.180	1.519
Slope/est. O.A.	1.07	1.10	1.04	1.08	1.16	1.20	1.34	1.43	1.21	1.26	1.48	1.44
Triangular cells												
Limiter and error norm	First order		GG-Barth		GG-directional		GG-Venkatakrisnan		LS-Venkatakrisnan		Structured Roe	
$1/\sqrt{(\text{No. of nodes})}$	L_1	L_2	L_1	L_2	L_1	L_2	L_1	L_2	L_1	L_2	L_1	L_2
5.42E-02	14.00	21.57	7.32	10.53	2.11	2.71	1.18	1.86	1.28	2.51	—	—
2.79E-02	6.76	10.56	3.57	5.63	0.74	1.09	0.64	0.92	0.27	0.47	—	—
1.42E-02	3.59	5.39	2.15	2.84	0.47	0.64	0.18	0.24	0.09	0.17	—	—
Slope/est. O.A.	1.02	1.04	0.91	0.98	1.13	1.08	1.43	1.52	1.97	2.02	—	—

Acknowledgments

The Numerical Aerodynamic Simulation Facility at NASA Ames provided computing support for much of this work, and this support is gratefully acknowledged. The authors would like to thank T. Barth, V. Venkatakrishnan, M. Berger, and W. K. Anderson for many insightful discussions and suggestions over the course of this research.

References

- ¹Barth, T. J., and Jespersen, D. C., "The Design and Application of Upwind Schemes on Unstructured Meshes," AIAA Paper 89-0366, Jan. 1989.
- ²Aftosmis, M., and Kroll, N., "A Quadrilateral-Based Second-Order TVD Method for Unstructured Adaptive Meshes," AIAA Paper 91-0124, Jan. 1991.
- ³Frink, N. T., Parikh, P., and Pirzadeh, S., "A Fast Upwind Solver for the Euler Equations on Three-Dimensional Unstructured Meshes," AIAA Paper 91-0102, Jan. 1991.
- ⁴Fursenko, A. A., Sharov, D. M., Timofeev, E. V., and Voinovich, P. A., "High-Resolution Schemes in Unstructured Grids in Transient Shocked Flow Simulation," *Lecture Notes in Physics 414, 13th International Conference on Numerical Methods in Fluid Dynamics*, 1993, pp. 250-255.
- ⁵Harten, A., "High Resolution Schemes for Hyperbolic Conservation Laws," *Journal of Computational Physics*, Vol. 49, 1983, pp. 357-393.
- ⁶van Leer, B., "Flux-Vector Splitting for the Euler Equations," Inst. for Computer Application in Science and Engineering, TR 82-30, Sept. 1982.
- ⁷Venkatakrishnan, V., "On the Accuracy of Limiters and Convergence to Steady State Solutions," AIAA Paper 93-0880, Jan. 1993.
- ⁸Barth, T. J., "A 3-D Least Squares Upwind Euler Solver for Unstructured Meshes," *Lecture Notes in Physics 414, 13th International Conference on Numerical Methods in Fluid Dynamics*, Springer-Verlag, 1993, pp. 240-244.
- ⁹Barth, T. J., "Aspects of Unstructured Grids and Finite-Volume Solvers for the Euler and Navier-Stokes Equations," AGARD Rept. 787, 1992.
- ¹⁰Barth, T. J., "Recent Developments in High Order K-Exact Reconstruction on Unstructured Meshes," AIAA Paper 93-0668, Jan. 1993.
- ¹¹Durlofsky, L. J., Engquist, B., and Osher, S., "Triangle Based Adaptive Stencils for the Solution of Hyperbolic Conservation Laws," *Journal of Computational Physics*, Vol. 98, 1992, pp. 64-73.
- ¹²Aftosmis, M., "Viscous Flow Simulation Using an Upwind Method for Hexahedral Based Adaptive Meshes," AIAA Paper 93-0772, Jan. 1993.
- ¹³Barth, T. J., "Numerical Aspects of Computing Viscous High Reynolds Number Flows on Unstructured Meshes," AIAA Paper 91-0721, Jan. 1991.
- ¹⁴Barth, T. J., and Frederickson, P. O., "Higher-Order Solution of the Euler Equations on Unstructured Grids Using Quadratic Reconstruction," AIAA Paper 90-0013, Jan. 1990.
- ¹⁵Godfrey, A. G., Mitchell, C. R., and Walters, R. W., "Practical Aspects of Spatially High Accurate Methods," AIAA Paper 92-0054, 1992.
- ¹⁶Coirier, W. J., and Powell, K. G., "An Accuracy Assessment of Cartesian-Mesh Approaches for the Euler Equations," AIAA Paper 93-3335, July 1993.
- ¹⁷Ni, R. H., "A Multiple-Grid Scheme for Solving the Euler Equations," *AIAA Journal*, Vol. 20, 1982, pp. 1565-1571.
- ¹⁸Boxer, E., Sterrett, J. R., and Wlodarski, J., "Application of Supersonic Vortex-Flow Theory to the Design of Supersonic Impulse Compressor- or Turbine-Blade Sections," NACA RM L52B06, 1952.
- ¹⁹Goldman, L. J., and Scullin, V. J., "Analytical Investigation of Supersonic Turbomachinery Blading I. Computer Program for Blading Design," NASA TN D-4421, 1968.
- ²⁰Tavares, T. S., "A Supersonic Fan Equipped Variable Cycle Engine for a Mach 2.7 Supersonic Transport," NASA-CR-177141, 1986.
- ²¹Gaitonde, D., and Shang, J., "Accuracy of Flux-Split Algorithms in High-Speed Viscous Flows," *AIAA Journal*, Vol. 31, No. 7, 1993, pp. 1215-1221.